

Journal of  
**Applied  
Crystallography**

ISSN 0021-8898

Editor: **Gernot Kosterz**

## **Orientation density function-controlled pole probability density function measurements: automated adaptive control of texture goniometers**

**Helmut Schaeben, Ralf Hielscher, Jean-Jacques Fundenberger, Daniel Potts and Jürgen Prestin**

Copyright © International Union of Crystallography

Author(s) of this paper may load this reprint on their own web site provided that this cover page is retained. Republication of this article or its storage in electronic databases or the like is not permitted without prior permission in writing from the IUCr.

# Orientation density function-controlled pole probability density function measurements: automated adaptive control of texture goniometers

Helmut Schaeben,<sup>a\*</sup> Ralf Hielscher,<sup>a</sup> Jean-Jacques Fundenberger,<sup>b</sup> Daniel Potts<sup>c</sup> and Jürgen Prestin<sup>d</sup>

<sup>a</sup>Geoscience Mathematics and Informatics, Freiberg University of Mining and Technology, Germany, <sup>b</sup>Laboratoire d'Etude des Textures et Application aux Matériaux, UMR CNRS 7078, Université de Metz, France, <sup>c</sup>Mathematics, Chemnitz University of Technology, Germany, and <sup>d</sup>Mathematics, Lübeck University, Germany. Correspondence e-mail: schaeben@geo.tu-freiberg.de

A novel control of a texture goniometer, which depends on the texture being measured itself, is suggested. In particular, it is suggested that the obsolete control with constant step sizes in both angles is replaced by an adaptive successive refinement of an initial coarse uniform grid to a locally refined grid, where the progressive refinement corresponds to the pattern of preferred crystallographic orientation. The prerequisites of this automated adaptive control is the fast inversion of pole intensities to orientation probabilities in the course of the measurements, and a mathematical method of inversion that does not require a raster of constant step sizes and applies to sharp textures.

© 2007 International Union of Crystallography  
Printed in Singapore – all rights reserved

## 1. Motivation and introduction

### 1.1. Crystallographic orientation

Texture analysis is the analysis of preferred crystallographic orientation in polycrystalline materials. Neglecting crystal symmetry or assuming triclinic crystal symmetry, the crystallographic orientation  $g$  of an individual crystal is the active orthogonal transformation  $g \in O(3)$  which brings an orthogonal coordinate system  $K_S = \langle \mathbf{x}, \mathbf{y}, \mathbf{z} \rangle$  fixed to the specimen into coincidence with an orthogonal coordinate system  $K_C = \langle \mathbf{a}, \mathbf{b}, \mathbf{c} \rangle$  fixed to the crystal,

$$g \in O(3) : K_S \mapsto K_C,$$

in the sense that

$$g \mathbf{x} = \mathbf{a}, \quad g \mathbf{y} = \mathbf{b}, \quad g \mathbf{z} = \mathbf{c}.$$

Then the vector  $\mathbf{r}_{K_S}$  of coordinates with respect to  $K_S$  of a unique vector  $\mathbf{v}$  and the vector  $\mathbf{h}_{K_C}$  of its coordinates with respect to  $K_C$  are related to one another by

$$g \mathbf{h}_{K_C} = \mathbf{r}_{K_S}.$$

It should be noted that handedness is not generally preserved.

In the case of crystal symmetry, several symmetrically equivalent crystal coordinate systems  $K_C, K'_C$  exist, which can be distinguished mathematically but not physically. If  $G_{\text{point}}$  denotes the point group of the crystal symmetry class, then the set of crystallographically equivalent orientations is represented by the coset  $g G_{\text{point}}$ . As a result of Friedel's law the effective crystal symmetry imposed by any diffraction experiment is described by the point group

$$G_{\text{Laue}} = G_{\text{point}} \otimes \{\text{id}, -\text{id}\},$$

which is also referred to as the Laue class (here  $\text{id}$  denotes the identity, and  $-\text{id}$  the inversion). Since

$$O(3)/G_{\text{Laue}} = \text{SO}(3)/[G_{\text{Laue}} \cap \text{SO}(3)],$$

the cosets of equivalent orientations with respect to the effective symmetry imposed by the diffraction experiment can be represented by proper rotations in  $\text{SO}(3)$  only. Therefore all considerations are restricted to  $\text{SO}(3)$ .

### 1.2. Orientation and pole probability density function

The major subject of texture analysis is the orientation probability density function (ODF)  $f$ , as it allows the determination of anisotropic macroscopic material properties from the corresponding single-crystal properties. More specifically, texture analysis is the analysis of patterns of preferred crystallographic orientation of a polycrystalline specimen given in terms of its orientation probability density function  $f: \text{SO}(3) \rightarrow g_+$  defined as

$$f(g) = \frac{V_g/V}{dg}, \quad (1)$$

where  $V$  denotes the total volume of the specimen,  $V_g$  the volume of crystallites carrying the orientation  $g$ , and  $dg$  the Haar measure on  $\text{SO}(3)$ . In order to model crystal symmetry given by a Laue group  $G_{\text{Laue}} \subset O(3)$ , the ODF  $f$  is defined to satisfy the symmetry relations

$$f(g) = f(gg'), \quad g' \in G_{\text{Laue}} \cap O(3).$$

With X-ray (including synchrotron) or neutron diffraction experiments, the orientation density  $f$  cannot be measured directly; only integral information concerning  $f$  can be sampled. More precisely, 'pole figures'

$$P(\mathbf{h}, \mathbf{r}) = \frac{1}{4\pi} \int_{G(\mathbf{h}, \mathbf{r}) \cup G(-\mathbf{h}, \mathbf{r})} f(g) dg, \quad (\mathbf{h}, \mathbf{r}) \in \mathbb{S}^2 \times \mathbb{S}^2 \quad (2)$$

are experimentally accessible with a texture goniometer for discrete directions  $\mathbf{h}_i, \mathbf{r}_{j_i} \in \mathbb{S}^2$ , where  $\mathbb{S}^2$  denotes the unit sphere in  $\mathbb{R}^3$ . The path of integration  $G(\mathbf{h}, \mathbf{r})$  is defined as the fibre

$$G(\mathbf{h}, \mathbf{r}) = \{g \in \text{SO}(3) \mid g\mathbf{h} = \mathbf{r}, (\mathbf{h}, \mathbf{r}) \in \mathbb{S}^2 \times \mathbb{S}^2\}.$$

Interpreting  $\mathbf{r}$  rather as a parameter than as a variable, the function  $\mathbf{h} \rightarrow P(\mathbf{h}, \mathbf{r})$  is the probability density function providing the probability that the crystallographic direction ('pole')  $\mathbf{h}$  statistically coincides with the macroscopic specimen direction  $\mathbf{r}$ .

The basic term of the mathematical model of texture goniometry is the one-dimensional totally geodesic Radon transform

$$\mathcal{R}f(\mathbf{h}, \mathbf{r}) = \frac{1}{2\pi} \int_{G(\mathbf{h}, \mathbf{r})} f(g) dg, \quad (\mathbf{h}, \mathbf{r}) \in \mathbb{S}^2 \times \mathbb{S}^2, \quad (3)$$

which associates to an orientation probability density function  $f$  on  $\text{SO}(3)$  its mean values along the one-dimensional geodesics  $G(\mathbf{h}, \mathbf{r})$  and

$$P(\mathbf{h}, \mathbf{r}) = \frac{1}{2} [\mathcal{R}f(\mathbf{h}, \mathbf{r}) + \mathcal{R}f(\mathbf{h}, -\mathbf{r})] = \mathcal{X}f(\mathbf{h}, \mathbf{r}), \quad (4)$$

which is called the basic crystallographic X-ray transform even though it does not depend on the radiation used for diffraction. Notationally, we do not distinguish between experimen-

tally accessible pole figures and the basic crystallographic X-ray transform, which differ just by a summation over crystallographically symmetrically equivalent directions.

### 1.3. Pole-to-orientation density inversion

In practice, the problem is to recover a reasonable approximation of the orientation probability density function  $f$  from experimental intensities

$$I_{ij} = I(\mathbf{h}_i, \mathbf{r}_{j_i}) = a(\mathbf{h}_i) P(\mathbf{h}_i, \mathbf{r}_{j_i}) + b(\mathbf{h}_i), \quad (5)$$

$$j_i = 1, \dots, J_i, \quad i = 1, \dots, I,$$

modelled by pole probability density functions (PDFs)  $P$  with constants  $a(\mathbf{h}_i), b(\mathbf{h}_i) \in \mathbb{R}$  depending on the crystal form. The indices indicate that there is no regular grid of positions  $(\mathbf{h}_i, \mathbf{r}_{j_i})$  imposed, but that the specimen positions  $\mathbf{r}_{j_i}$  may depend on the crystal form  $\mathbf{h}_i$  and may be different for each crystal form.

From integral geometry it is well known that the totally geodesic Radon transform possesses a unique inverse under mathematically mild assumptions (*cf.* Helgason, 1984, 1999). As a result of the additional symmetry introduced by the diffraction experiment itself, the basic crystallographic X-ray transform is not generally invertible, and therefore neither are the pole probability density functions (Matthies, 1979). To resolve the inverse problem of texture analysis, additional modelling assumptions are required. Here we apply a first modelling assumption that the true orientation probability density function  $f: \text{SO}(3) \rightarrow \mathbb{R}_+$  be expanded into a finite series of given radially symmetric basis functions, the Radon transform of which is analytically known.

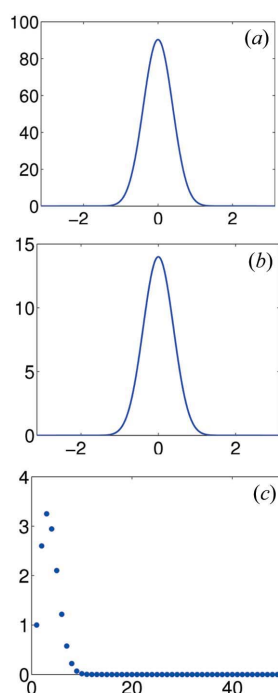


**Figure 1**  
The de la Vallée Poussin kernel for  $\kappa = 13$  (a), its Radon transform (b) on the spatial domain and their spectral representation on the frequency domain (c).

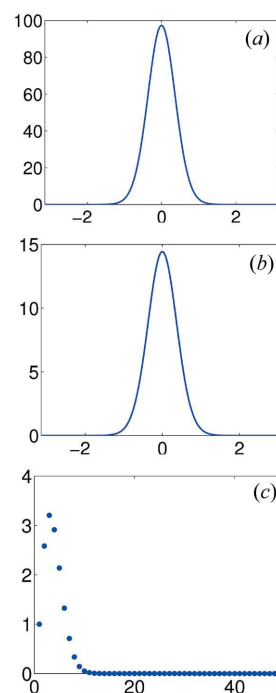


**Figure 2**  
The von Mises-Fisher kernel for  $\kappa = 7.5$  (a), its Radon transform (b) on the spatial domain and their spectral representation on the frequency domain (c).

## research papers

To be more precise, let

$$\psi(g) = \tilde{\psi}[\omega(gg_0^{-1})], \quad \omega(gg_0^{-1}) = \arccos \frac{\text{trace } gg_0^{-1} - 1}{2}, \quad (6)$$

be a non-negative, radially symmetric function on  $\text{SO}(3)$ , well localized around its centre  $g_0 \in \text{SO}(3)$  that is monotonously decreasing with respect to the angular distance  $\omega(g, g_0)$  of  $g$  from  $g_0$ . Then the half-width  $b \in (0, 1)$  of  $\psi$  is defined by

$$\tilde{\psi}(b) = \frac{1}{2} \tilde{\psi}(0).$$

Furthermore, let  $g_1, \dots, g_M \in \text{SO}(3)$  be an approximate equidistribution in  $\text{SO}(3)$  with resolution  $\delta = \min_{m \neq m'} \omega(g_m g_{m'}^{-1})$ . Then we apply the first model assumption that there are coefficients  $\mathbf{c} \in \mathbb{R}_+^M$  such that

$$f(g) \simeq \sum_{m=1}^M c_m \psi[\omega(gg_m^{-1})]. \quad (7)$$

Examples of suitable radially symmetric functions are the *de la Vallée Poussin kernel*

$$\tilde{\psi}_\kappa(\omega) = \frac{B(\frac{3}{2}, \frac{1}{2})}{B(\frac{3}{2}, \kappa + \frac{1}{2})} \cos^{2\kappa}(\omega/2), \quad \omega \in (0, \pi), \quad \kappa \in \mathbb{R}, \quad (8)$$

where  $B$  denotes the  $\beta$  function, and the *von Mises–Fisher kernel*

$$\tilde{\psi}_\kappa(\omega) = \frac{1}{\mathcal{I}_0(\kappa) - \mathcal{I}_1(\kappa)} \exp(\kappa \cos \omega), \quad \omega \in [0, \pi],$$

where  $\mathcal{I}_n, n \in \mathbb{N}_0$  denote the modified Bessel functions of the first kind,

$$\mathcal{I}_n(\kappa) = \frac{1}{\pi} \int_0^\pi \exp(\kappa \cos \omega) \cos n\omega \, d\omega, \quad \kappa \in \mathbb{R}_+.$$

The de la Vallée Poussin kernel is of special interest as its Fourier coefficients not only decrease smoothly, but also eventually vanish, *i.e.* its harmonic series expansion is finite. Moreover, its form is preserved under the Radon transform, *i.e.* the Radon transform of the de la Vallée Poussin kernel on  $\mathbb{S}^2 \times \mathbb{S}^2$  (Schaeben, 1997, 1999; Hielscher, 2007). It is well known that radial symmetry is preserved by the Radon transform. Then, from a practical point of view it seems sensible to choose radially symmetric basis functions that are easily numerically tractable. For both kernel functions mentioned above there are simple explicit formulae for their Radon transforms, *i.e.* we have

$$\mathcal{R}\psi_\kappa(\mathbf{h}, \mathbf{r}) = (1 + \kappa) \cos^{2\kappa} \angle(g_0 \mathbf{h}, \mathbf{r})/2$$

in the case of the de la Vallée Poussin kernel and

$$\begin{aligned} \mathcal{R}\psi_\kappa(\mathbf{h}, \mathbf{r}) &= \frac{\mathcal{I}_0\{\frac{\kappa}{2}[1 + \cos \angle(g\mathbf{h}, \mathbf{r})]\}}{\mathcal{I}_0(\kappa) - \mathcal{I}_1(\kappa)} \\ &\times \exp\left\{\frac{\kappa}{2}[-1 + \cos \angle(g\mathbf{h}, \mathbf{r})]\right\} \end{aligned}$$

in the case of the von Mises–Fisher kernel.

Plots of the de la Vallée Poussin kernel and the von Mises–Fisher kernel are given in Figs. 1 and 2.

Since the Radon transform is linear, its application to the superposition of radially symmetric functions described in equation (7) results in

$$\mathcal{R}f(\mathbf{h}, \mathbf{r}) = \sum_{m=1}^M c_m \mathcal{R}\psi_\kappa(g_m \mathbf{h}, \mathbf{r}).$$

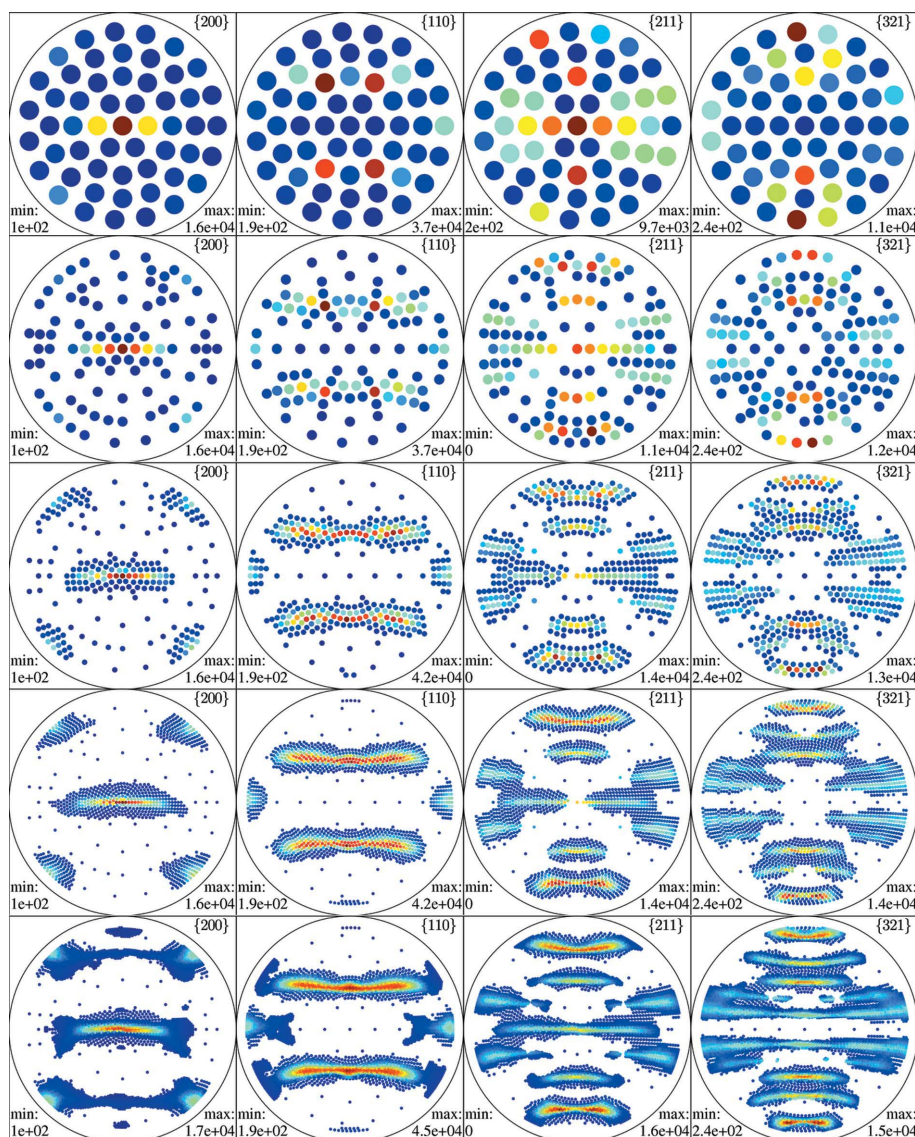


**Figure 3** Successive refinement of measurement positions in  $k$  steps, where  $k$  enumerates the rows.

The numerical resolution of the inverse Radon transform is accomplished by fitting the coefficients  $c_m, m = 1, \dots, M$ , to the measured intensities subject to the additional modelling assumptions that  $c_m \geq 0, k = 1, \dots, M$ , to guarantee non-negativity.

Since the inverse of the basic crystallographic X-ray transform is not well defined, we introduce as yet another modelling assumption the maximum smoothness of the orientation probability density function to be recovered. Here we suggest the measurement of smoothness in terms of derivatives of  $f$ , or more generally in terms of norms of  $f$  with respect to appropriately constructed Sobolev spaces  $\mathcal{H}[\text{SO}(3)]$  (Hielscher *et al.*, 2005). The nonlinear problem to be solved then reads

$$\tilde{c} = \operatorname{argmin} \sum_{i=1}^I \sum_{j=1}^{J_i} \left\| \sum_{m=1}^M a(\mathbf{h}_i) c_m \mathcal{R} \psi_{\kappa}(\mathbf{g}_m \mathbf{h}_i, \mathbf{r}_{j_i}) + b(\mathbf{h}_i) - \iota_{ij} \right\|^2 + \lambda \left\| \sum_{m=1}^M c_m \psi_{\kappa}(\circ \mathbf{g}_m^{-1})_{\mathcal{H}[\text{SO}(3)]} \right\|^2, \quad (9)$$

where  $\lambda$  is the parameter of regularization weighting the penalty term.

To solve equation (9), methods of fast matrix-vector multiplication are combined with iterative methods. Fast Fourier transforms are an option for the fast matrix-vector multiplication; alternatively, multipole or multigrid methods

may be used. The modified steepest descent algorithm provides an iterative solution for the nonnegative constrained optimization problem, and so do the Richardson–Luci, gradient projection residual norm (GPRN) and gradient projection residual norm conjugated gradients (GPRNCG) methods (*cf.* Bardsley & Vogel, 2003).

The method may be seen as a generalization of the classical harmonic method initialized by Bunge (1965) and Roe (1965) and discussed by Schaeben (2000), or the texture component fit method (Grewen & Wassermann, 1955; Virnich *et al.*, 1978; Lücke *et al.*, 1981, 1986; Bukharova & Savyolova, 1985*a,b*; Nikolayev *et al.*, 1992; Helming & Eschner, 1990; Eschner, 1993, 1994), depending on the point of view (Schaeben & Boogaart, 2003). While a preliminary sketch was presented by Schaeben (1996) and Hielscher & Schaeben (2006), the method is fully developed by Hielscher (2007). It should be noted that our generalization may expand an orientation probability density function into up to 300 000 symmetrized radially symmetric basis functions, each with a half-width of  $1.5^\circ$ . It does not require a raster of constant step sizes for the measured intensities and applies to extremely sharp textures. The method will be comprehensively presented elsewhere in a forthcoming paper.

## 2. Automated adaptively controlled texture goniometry

In what follows,  $(hkl)$  are the Miller indices of a crystallographic lattice plane with normal vector  $\mathbf{h}$ , and  $\{hkl\}$  denotes the crystal form of lattice

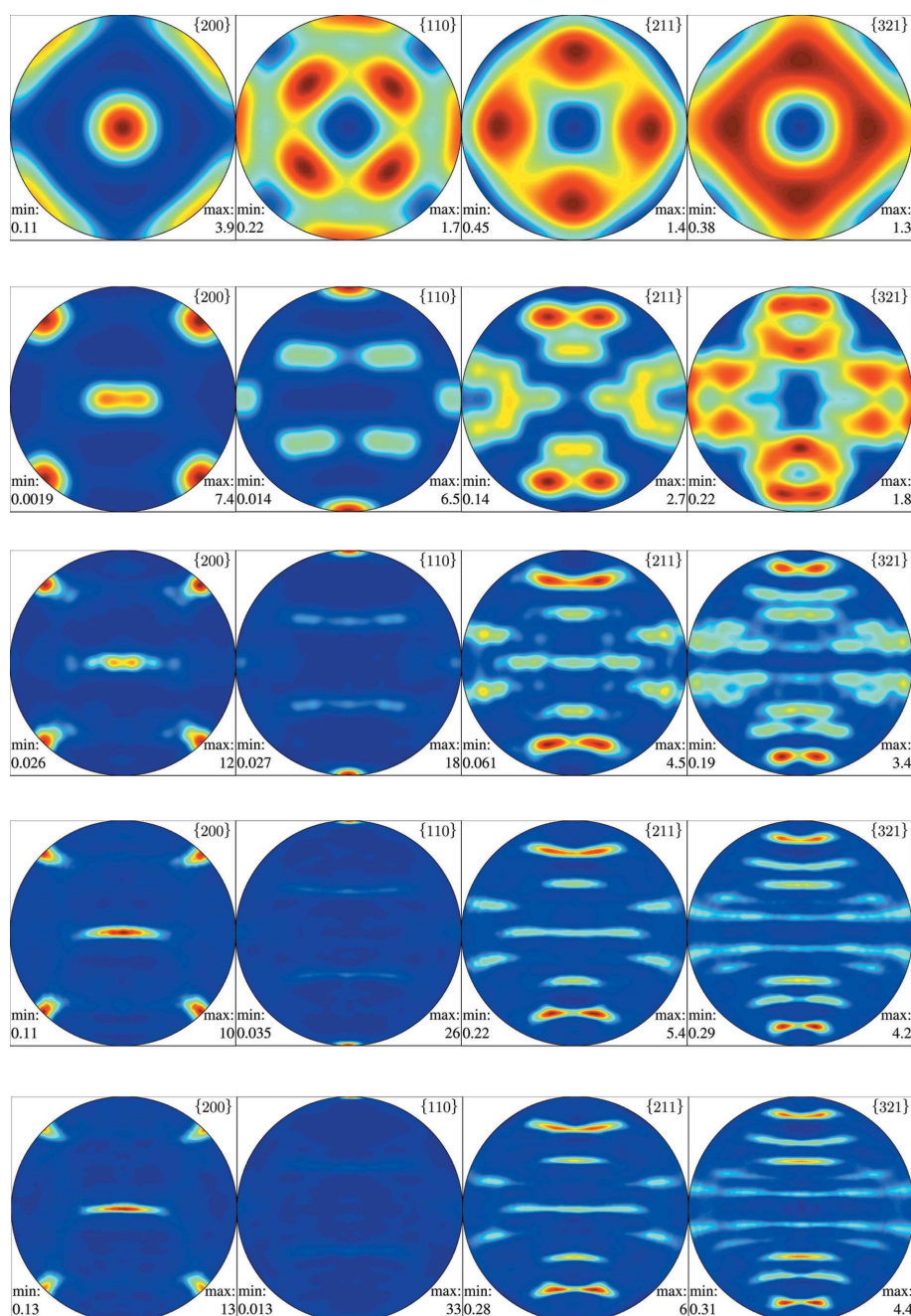


**Figure 4** Computed PDFs after the  $k$ th turn of measurement, where  $k$  enumerates the rows.

planes symmetrically equivalent to  $\{hkl\}$ .

Texture analysis employs the effect of diffraction of radiation (X-rays including synchrotron, neutrons, electrons) at the crystallographic lattice planes. It is based on the Bragg equation

$$n\lambda = 2d_{\{hkl\}} \sin \vartheta_{\{hkl\}}, \quad n \in \mathbb{N}.$$

For a monochromatic beam of wavelength  $\lambda$  and a constant  $\vartheta_{\{hkl\}}$ , the diffracted intensity is a measure of the volume portion of crystals for which the bisecting line between the initial and diffracted beam is orthogonal to lattice planes with lattice spacing  $d_{\{hkl\}}$ . Then the diffracted intensity recorded with a conventional detector is a statistical measure of the frequency by volume that a given crystallographic direction agrees with a given specimen direction  $\mathbf{r} \in \mathbb{S}^2$ . With a diffractometer with a texture goniometer, the specimen can be

rotated in such a way that each normal  $\mathbf{h}$  of lattice planes with spacing  $d_{\{hkl\}}$  satisfies this condition once. Thus, the diffraction experiment results for a lattice plane given in terms of its Miller indices  $\{hkl\}$  in a statistical distribution of intensities  $P(\mathbf{h}, \mathbf{r})$  on the  $\{hkl\}$ -pole sphere, which is referred to as the  $\{hkl\}$ -pole figure in texture analysis.

In the early days of texture analysis, the rotation of the specimen with the texture goniometer used to be controlled by step motors such that intensity measurements were performed with respect to a regular raster of measuring positions with a constant step size  $\Delta\varphi$  in the azimuth  $\varphi$  and a constant step size  $\Delta\chi$  in the pole (tilt) angle  $\chi$ , or with respect to a regular raster of measuring positions with a constant step size along a spiral. Thus the specimen directions of measurements are geometrically arranged in a regular grid, with the former control in a grid of points

$$\begin{aligned} \mathbf{r}_{ij} = & (\sin i \Delta\varphi \sin j \Delta\chi, \\ & \cos i \Delta\varphi \sin j \Delta\chi, \cos j \Delta\chi)^t, \\ i = & 0, 1, \dots, \left(\frac{2\pi}{\Delta\varphi}\right), \\ j = & 0, 1, \dots, \left(\frac{\pi}{2\Delta\chi}\right). \end{aligned} \quad (10)$$

With  $\Delta\varphi = \Delta\chi = 5^\circ$ , an incompletely measured pole figure with  $0 \leq \varphi \leq 360^\circ$ ,  $0 \leq \chi \leq 70^\circ$  comprises 1008 positions of measurements. Nowadays the rotation of the specimen is controlled by a step motor and a personal computer. However, the major features of the experiment have been conserved: (i) the sequence of positions is fixed before the experiment is started and thus independent of the progress of the measurements, and (ii) the measurements are geometrically arranged in a regular grid. An obviously poor property of this kind of regular grid is the varying spatial resolution of the pole sphere. Presumably, regular grids of the type represented by equation (10) are still used because commercial software packages for texture analysis accompanying diffractometers with a texture goniometer require data confined to such grids, even though more appropriate grids, in particular approximately spherically uniform grids, have been suggested and successfully applied in practical tests (Tarkowski *et al.*, 2004).

Traditionally, the single most prominent goal of texture analysis is to recover a reasonable approximation  $\hat{f}$  of the orientation probability density

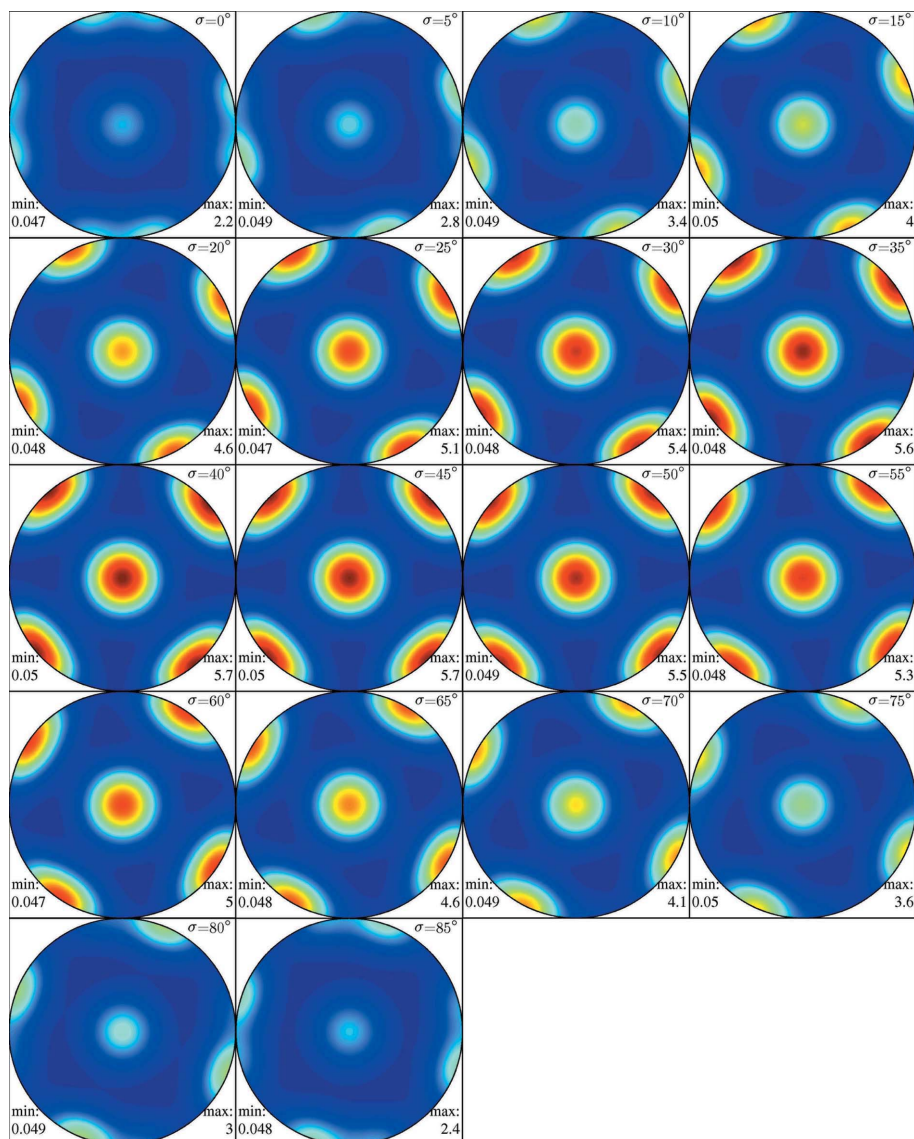


**Figure 5**  
Estimated ODF after initial measurements.

function  $f$  from experimental pole-figure intensities  $I$ , cf. equation (5). Usually an orientation probability density  $\tilde{f}$  is computed after the experiment is finished.

Alternatively, we suggest a novel control of a texture goniometer which depends on the texture being measured itself. In particular, we suggest replacing the obsolete control with constant step sizes in both angles by an adaptive successive refinement of an initial coarse uniform grid to a locally refined grid where the progressive refinement corresponds to the pattern of preferred crystallographic orientation. Hence, our novel control differs in two essentials from the conventional control: (i) the sequence of positions is not fixed but incomplete when the experiment is started and depends on the progress of the experiment, and (ii) the successive refinement of positions depends on the actually observed pattern of preferred crystallographic orientation and its simultaneous analysis in terms of successively improved approximations of the orientation probability density function

with respect to the most recent refinement, and does not result in a regular grid. Thus measurements and computations of orientation probability density functions are mutually dependent. The prerequisite of this automated adaptive control is the fast inversion of experimental pole intensities to mathematically modelled orientation probabilities in the course of the measurements, and a mathematical method of inversion that does not require a raster of constant step sizes and which applies to sharp textures. The automated adaptive control of the texture goniometer is especially well suited for the capture, mathematical representation and analysis of sharp textures.

The experiment commences with a list of initial positions according to a coarse approximately uniform grid. This list is processed by the personal computer controlling the texture goniometer and directed to the step motor. During the first turn of measurements intensities with respect to this initial grid of positions are recorded. These pole-figure intensities are

inverted to the initial approximation of an orientation probability density function according to the method given by equation (9). This first approximation is analysed to determine regions of the  $h$ -pole spheres of special interest where the initial grid should be refined locally. Criteria for refinement may be

(i) values of the computed pole probability density function larger than a user-defined threshold,

(ii) a difference of measured and computed pole probability density functions larger than a user-defined threshold,

(iii) values of the gradient of the computed pole probability density function larger than a user-defined threshold,

(iv) values of the Laplacian of the computed pole probability density function larger than a user-defined threshold, or

(v) any other sensible property.

The value of the threshold may be constant or change with the turn of the measurements. The criteria may be chosen alternatively or may be combined in an hierarchical or weighted manner.

The additional positions of the locally refined grid are then added to the list of positions controlling the texture goniometer and directed to the step motor. In the second turn of measurements, intensities with respect to these additional positions are recorded. Depending on the construc-

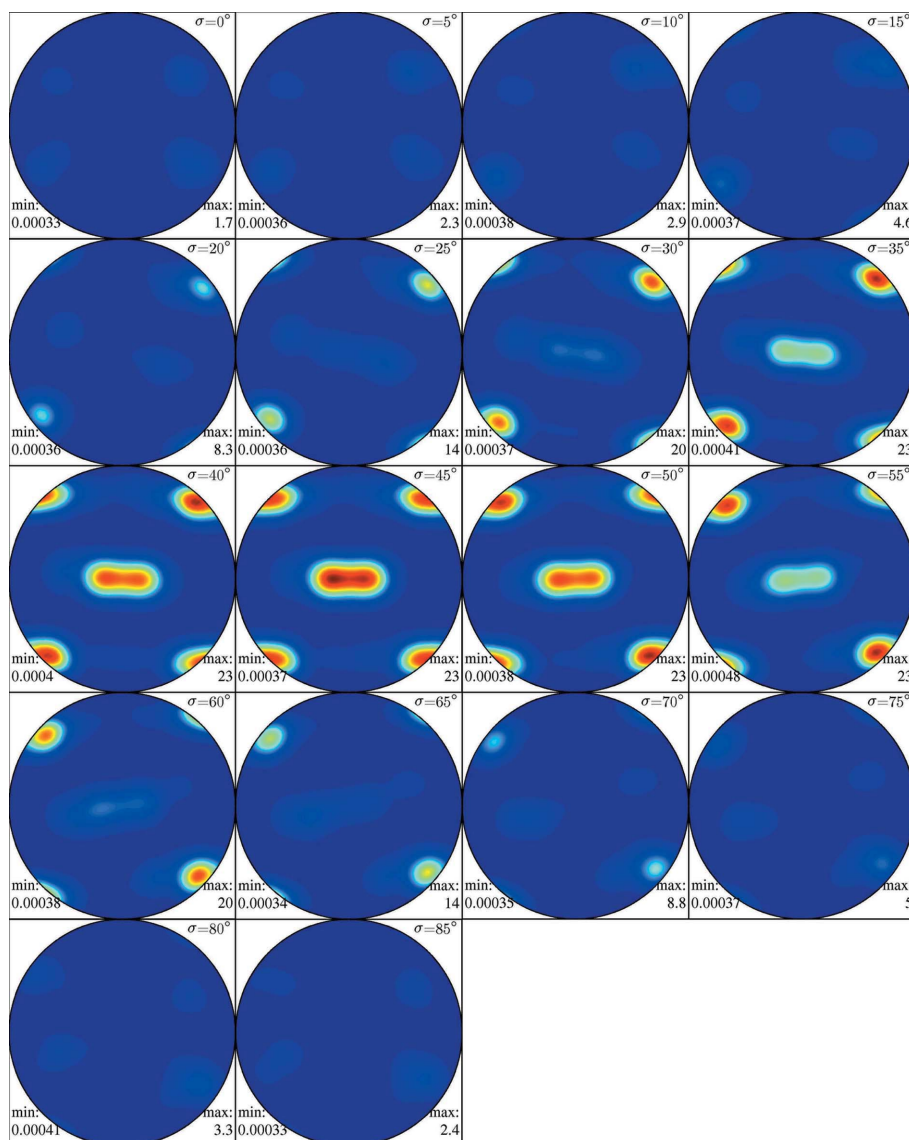


**Figure 6**  
Estimated ODF after the first refinement.

tion of the diffractometer and the goniometer, the sequence of the positions may be optimized to minimize the total motion of the specimen or the total time of the second turn. The new intensities are entered into the inversion and start the computation of an improved approximation of an orientation probability density function. The first computed approximation is now used as initial solution of the optimization problem given by equation (9). Its renewed analysis results in an updated local refinement or in a progressive local refinement of the same regions of the pole spheres. These new positions are again added to the list of positions, and the experiment is continued by a third turn of measurements with respect to these additional positions. The turns of measurement and computations are terminated if

- (i) the criteria for refinement are exhausted,
- (ii) the approximation of an orientation probability density function cannot be improved, or
- (iii) the technical limitations of the diffractometer or the texture goniometer are reached.

The advantage of this automated adaptive control is an efficient experimental design. More specifically, our design provides a maximum of information within a minimum period of time or an optimum use of the available period of time for measurements. Finally, extremely sharp textures can be efficiently captured, represented and analysed with this approach. In the case of a ‘technical single crystal’, an efficient starting grid would be a very coarse grid already locally refined in a sufficiently large neighbourhood of the expected peak position (and its crystal symmetry equivalents), which is usually known *a priori*.

### 2.1. Flow chart

- (1) Choose crystal directions  $\mathbf{h}_1, \dots, \mathbf{h}_N \in \mathbb{S}^2$  for pole-figure measurements.
- (2) Initialize  $k \leftarrow 0$ .
- (3) Set initial resolution  $\delta^{(k)}$ .
- (4) Define initial coarse grid of specimen directions  $\mathbf{r}_{ij}^{(k)} \in \mathbb{S}^2, i = 1, \dots, N, j_i = 1, \dots, J_i^{(k)}$  with resolution  $\delta^{(k)}$ .
- (5) Measure diffraction intensities  $l_{ij}^{(k)}, i = 1, \dots, N, j_i = 1, \dots, J_i^{(k)}$ .
- (6) Estimate ODF  $f^{(k)}$  by solving PDF-to-ODF inversion problem.

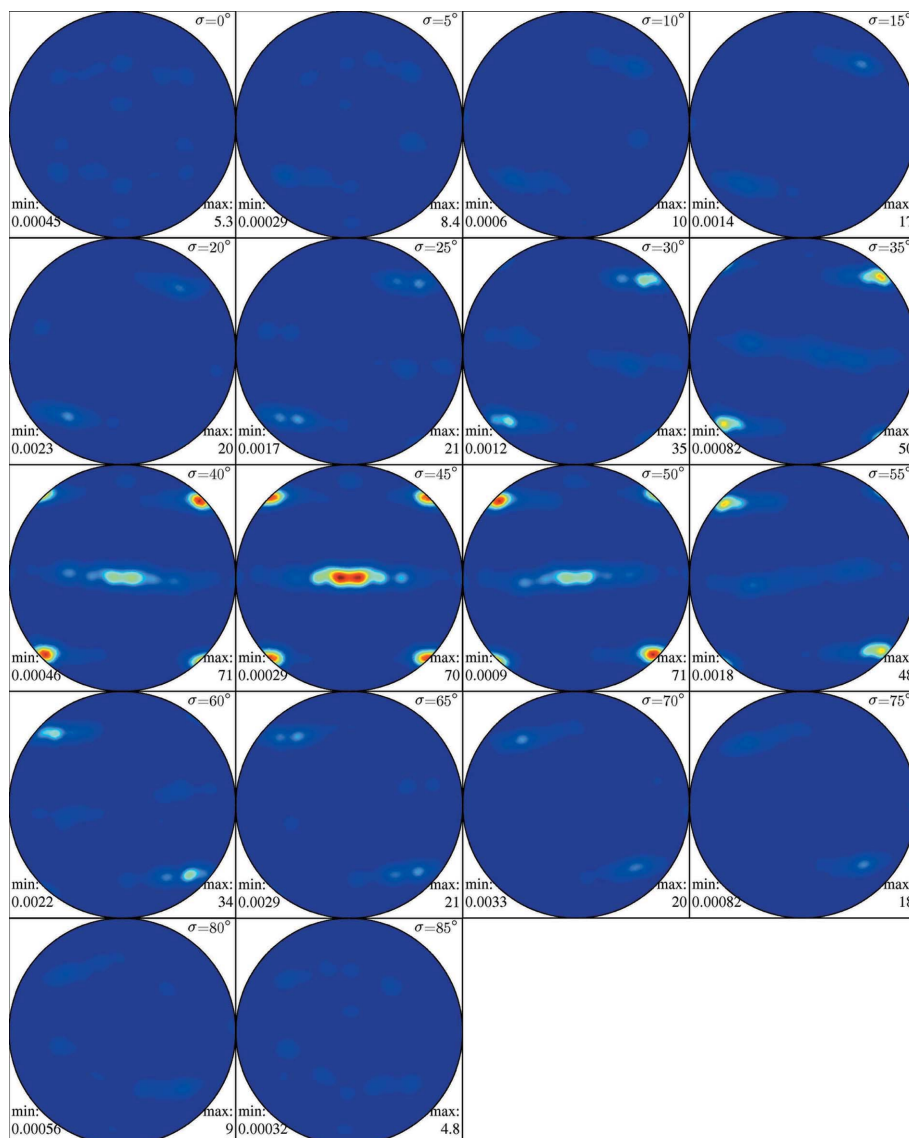


**Figure 7**  
Estimated ODF after the second refinement.

Fix an approximate equidistribution  $g_1^{(k)}, \dots, g_{M_k}^{(k)}$  in  $SO(3)/G_{\text{Laue}}$  with resolution  $\frac{3}{2}\delta^{(k)}$ .

Fix a radially symmetric function  $\psi_\kappa$  with half-width  $b = \delta^{(k)}$ .

Determine coefficients  $c_m^{(k)}, m = 1, \dots, M^{(k)}$  of the *ansatz* [equation (7)] by solving the minimization problem equation (9).

(7) Stop if termination criteria are satisfied, *e.g.* if the maximum resolution of the texture goniometer is reached or the estimate  $f^{(k)}$  sufficiently explains the texture.

(8) Refine resolution  $\delta^{(k+1)} = \frac{1}{2}\delta^{(k)}$ .

(9) Define grids of specimen directions  $\mathbf{r}_{ij}^{(k+1)} \in \mathbb{S}^2, i = 1, \dots, N, j_i = 1, \dots, J_i^{(k+1)}$ , with resolution  $\delta^{(k+1)}$  by refining the grids  $\mathbf{r}_{ij}^{(k)} \in \mathbb{S}^2, i = 1, \dots, N, j_i = 1, \dots, J_i^{(k)}$ .

(10) Calculate criteria of refinement for all new specimen directions  $\mathbf{r}_{ij}^{(k+1)} \in \mathbb{S}^2, i = 1, \dots, N, j_i = 1, \dots, J_i^{(k+1)}$  (*e.g.* lower bound for computed PDF, gradient of the PDF at these directions *etc.*) based on the current estimate of the ODF  $f^{(k)}$ .

(11) Omit all points of the refined grids  $\mathbf{r}_{ij_i}^{(k+1)} \in \mathbb{S}^2$ ,  $i = 1, \dots, N$ ,  $j_i = 1, \dots, J_i^{(k+1)}$ , that do not satisfy the refinement criteria.

(12) Set  $k \leftarrow k + 1$  and continue with step 5.

### 3. Practical example

The automated adaptive control of the texture goniometer, in particular its geometrical elements of successive local refinement of the specimen directions for which intensities are to be measured, will be presented and explained with the following case study. We analyse a molybdenum specimen with cubic crystal symmetry  $G_{\text{cub}}$  with a Siemens–Bruker D5000 diffractometer with a Huber goniometer, restricting ourselves to the four crystal forms  $\{hkl\} = \{200\}, \{110\}, \{211\}, \{321\}$ .

Starting with the initial resolution  $\delta^{(1)} = 20^\circ$ , we construct approximate equidistributions of specimen directions  $\mathbf{r}_{ij_i}^{(1)} \in \mathbb{S}^2$ ,  $i = 1, \dots, 4$ ,  $j_i = 1, \dots, 54$ , with maximum azimuth angle  $\chi = 80^\circ$ . The maximum azimuth angle is a result of restrictions of the experimental design. Using the ability of the goniometer to measure diffraction intensities for arbitrary arrangements of specimen directions, we determine diffraction data  $(l_{ij_i}^{(1)}, \mathbf{h}_i, \mathbf{r}_{ij_i}^{(1)})$ ,  $i = 1, \dots, 4$ ,  $j_i = 1, \dots, 54$ . These data are plotted in the first row of Fig. 3.

Following the flow chart of the automated adaptive control algorithm, we fix an approximate equidistribution  $\mathbf{g}_1^{(1)}, \dots, \mathbf{g}_{204}^{(1)}$  in  $\text{SO}(3)/G_{\text{cub}}$  with resolution  $\frac{3}{2}\delta^{(1)} = 30^\circ$ . As *ansatz* function  $\psi^{(1)}$ , we choose the de la Vallée Poussin kernel with half-width  $b^{(1)} = 20^\circ$ . Now the PDF-to-ODF inversion algorithm is applied and a first estimated ODF  $\hat{f}^{(1)}$  is obtained as a linear combination of the *ansatz* function  $\psi^{(1)}$  shifted into the grid rotations  $\mathbf{g}_1^{(1)}, \dots, \mathbf{g}_{204}^{(1)}$ . A plot of this ODF is given in Fig. 5. Plots of computed pole figures can be found in the top row of Fig. 4.

These computed pole figures are used in the refinement step to define a grid of additional specimen directions  $\mathbf{r}_{ij_i}^{(2)} \in \mathbb{S}^2$ ,  $i = 1, \dots, 4$ ,  $j_i = 1, \dots, N_i^{(2)}$ , individually for each pole figure. For this purpose each initial grid is refined to have the resolution  $\delta^{(2)} = \frac{1}{2}\delta^{(1)} = 10^\circ$ , but then only those specimen directions are retained for which the value of the computed PDF exceeds the threshold value of 1.

Next, diffraction intensities  $(l_{ij_i}^{(2)}, \mathbf{h}_i, \mathbf{r}_{ij_i}^{(2)})$ ,  $i = 1, \dots, 4$ ,  $j_i = 1, \dots, N_i^{(2)}$ , with respect to the additional specimen

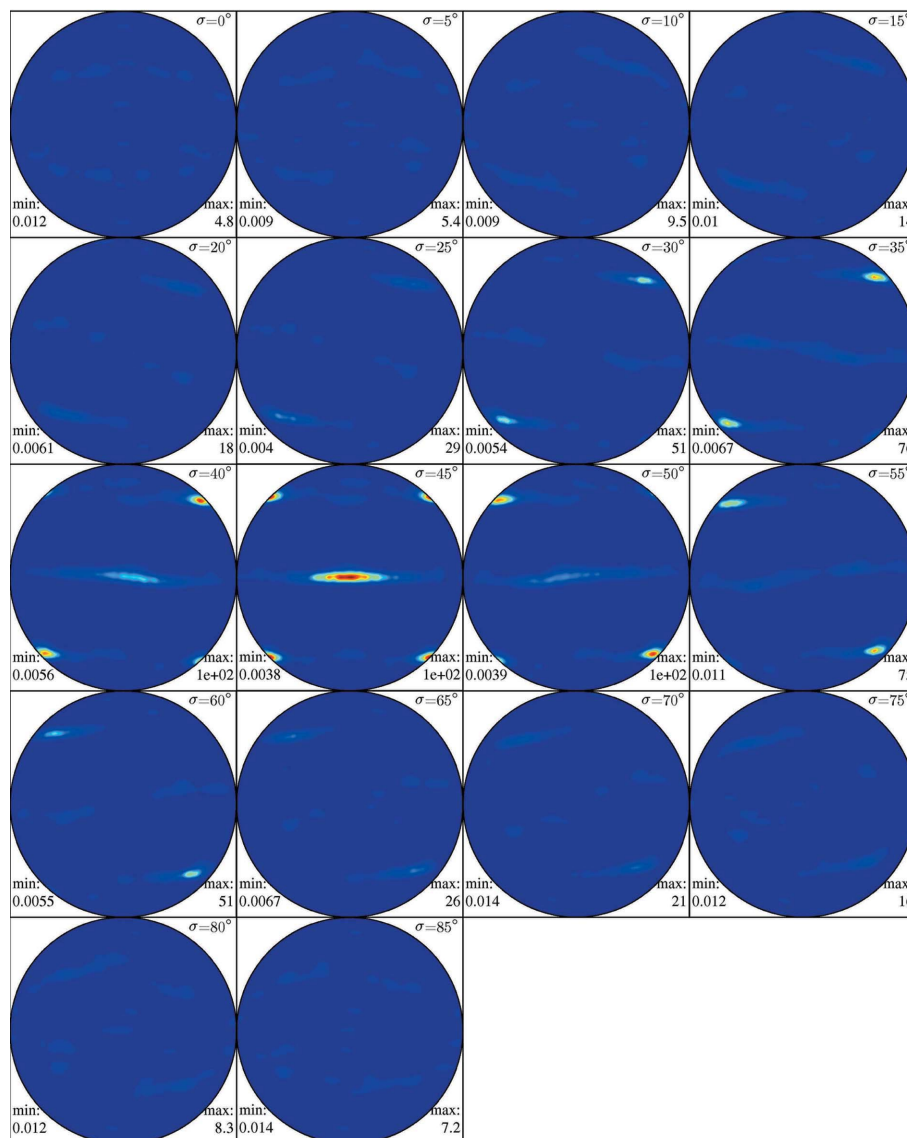


**Figure 8**  
Estimated ODF after the third refinement.

directions are measured. A plot of these together with previously measured diffraction intensities can be found in the second row of Fig. 3. Successive calculations of estimations of the ODF, refinements of the grid of specimen directions, and measurements of the corresponding diffraction intensities result in progressively refined sets of diffraction data  $(l_{ij_i}^{(k)}, \mathbf{h}_i, \mathbf{r}_{ij_i}^{(k)})$ ,  $i = 1, \dots, 4$ ,  $j_i = 1, \dots, N_i^{(k)}$ ,  $k = 1, \dots, 5$ , plotted in Fig. 3, and progressively refined ODF estimates  $\hat{f}^{(1)}, \dots, \hat{f}^{(5)}$ . The estimated ODFs are plotted in Figs. 5–9, and the computed pole figures are plotted in Fig. 4. In order to plot ODFs, we use  $\sigma$  sections as described by Helming *et al.* (1988). More precisely, any individual section of the ODF  $f$  is a spherical plot of the function  $(\alpha, \beta) \mapsto f(\alpha, \beta, \sigma - \alpha)$  with a fixed value for  $\sigma$ . Here  $(\alpha, \beta, \gamma)$  denote the Euler angle representation of a rotation according to the conventions used by Helming *et al.* (1988).

In Table 1 the parameters of the individual steps are summarized. The first column displays the angular resolution  $\delta$

**Table 1**

Parameters for single refinement and recalculation steps.

Included are the resolution  $\delta$  of the grid of specimen directions of  $\mathbb{S}^2$ , the cumulative total number  $\bar{N}$  of measured diffraction intensities with respect to the locally refined grids, the total number  $\bar{N}_{\text{reg}}$  of diffraction intensities to be measured in a conventional experiment with a regular grid, the cumulative measurement time, the total number  $M$  of *ansatz* functions involved in the PDF-to-ODF inversion problem, the maximum order of harmonic series expansion (bandwidth)  $L$  of the *ansatz* functions, and the computational time to solve the PDF-to-ODF inversion problem with Core 2 Duo c.p.u. with 186 GHz c.p.u. frequency and 2 Gbyte RAM.

Step	$\delta$ (°)	$\bar{N}$	$\bar{N}_{\text{reg}}$	Measurement time (h)	$M$	$L$	C.p.u. time
1	20	216	288	0.60	21	23	3 s
2	10	443	1152	1.23	204	52	28 s
3	5	1621	4608	4.50	1493	108	209 s
4	2.5	5511	18432	15.30	11767	215	1600 s
5	1.25	19191	73728	53.30	94040	432	31 h

of the grid of specimen directions  $\mathbf{r}_{ij}^{(k)}$  used in step  $k = 1, \dots, 5$ , and the second column displays the resulting total number  $\bar{N}$  of measured diffraction intensities with respect to the locally refined grids. This total number of measured intensities is compared with the total number  $\bar{N}_{\text{reg}}$  of specimen directions for a conventional, regular grid on the hemisphere  $\mathbb{S}_+^2$  displayed in the third column. The cumulative time spent to perform the measurements up to each step is displayed in the fourth column. Since the measurement time almost linearly increases with the number of measured diffraction intensities, we conclude that we have time savings of up to 75% or 150 h (step five). The time savings of about 40% in the third step of the successive refinement corresponds almost exactly to the time savings observed previously (Tarkowski *et al.*, 2004) when comparing equal-angle and equal-area, *i.e.* approximately uniform grids.

The fifth column displays the number  $M^{(k)}$  of *ansatz* functions  $\psi_k[\circ(\mathbf{g}_m^{(k)})^{-1}]$ ,  $m = 1, \dots, M^{(k)}$ , used for the representation of the ODF estimate  $\hat{f}^{(k)}$  in step  $k$ . In column six the maximum order of the harmonic series expansion,  $L^{(k)}$  ('bandwidth') is specified to which the *ansatz* functions are restricted to allow for fast Fourier techniques. The computational time for the PDF-to-ODF inversion was measured on a notebook with Intel Core 2 Duo processor with 1.86 GHz c.p.u. frequency and 2 Gbyte of memory. Obviously, the computational time is negligible compared with the time savings during the measurement process.

It should be noted that the c.p.u. time increases by a factor of  $2^3 = 8$  from one refinement to the next, except for the last refinement, as it depends only on the spatial resolution of the grid of  $\text{SO}(3)$  which is successively doubled, and not on the total number of measured intensities  $\bar{N}$ . In the last step, a lack of memory caused additional computations and memory swapping. With sufficiently large memory the c.p.u. time could be reduced from 31 h to approximately 4 h.

#### 4. Conclusions

Using a novel method of PDF-to-ODF inversion and an implementation employing fast Fourier transform algorithms, we have removed obsolete restrictions such as seriously bounded series expansion degree, seriously

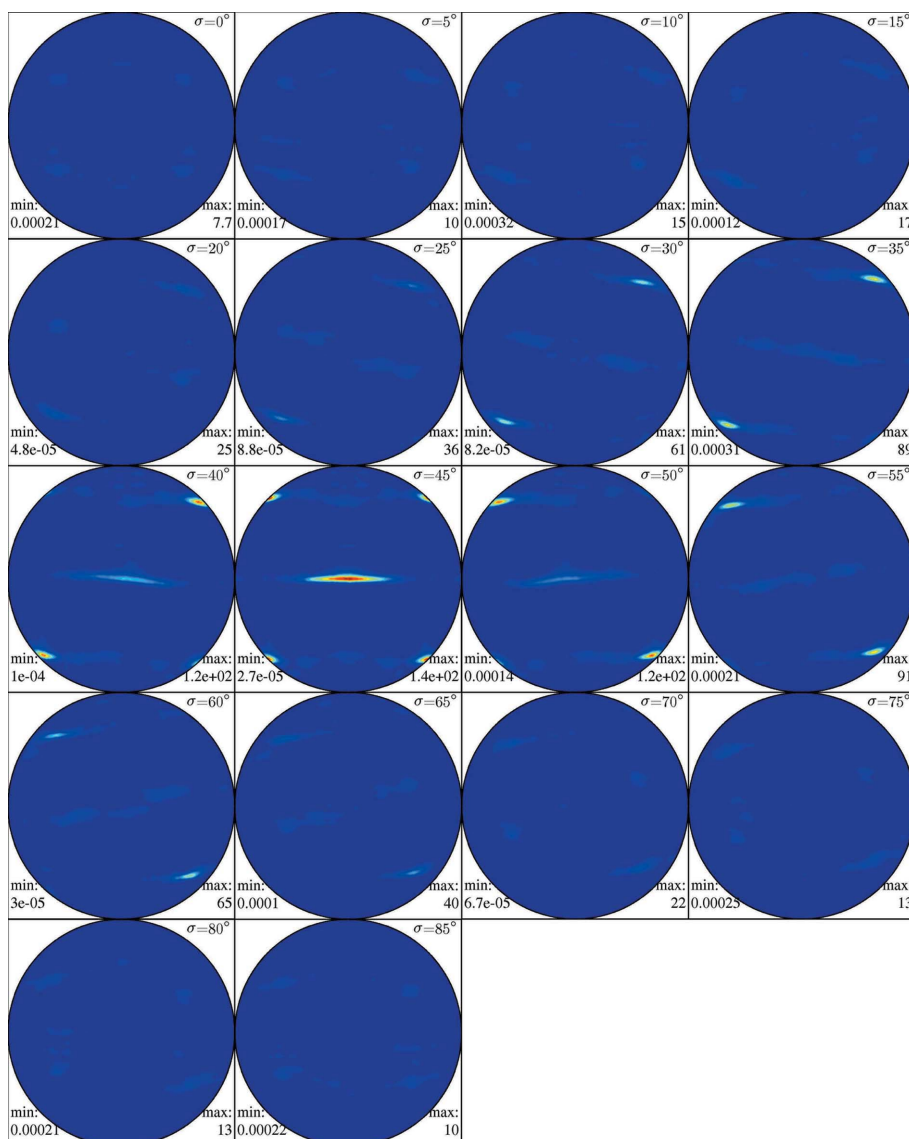


**Figure 9**

Estimated ODF after the fourth refinement.

bounded total number of components, regular spherical grid of measurements on the pole sphere, weak to moderate textures, and large c.p.u. times. Since it is now possible to process intensity data of arbitrary location on the pole sphere and successively compute numerical approximations of an ODF, explaining the data while making measurements, we suggest an automated adaptive control of a texture goniometer which either largely decreases the measuring time or makes best use of the available measuring time. This technique is especially well suited to the capture, representation and analysis of extremely sharp textures, as in technical single crystals.

The authors, in particular RH, gratefully acknowledge financial support by Deutsche Forschungsgemeinschaft (grant 'high resolution texture analysis', PR 331/11, SCHA 465/15).

## References

- Bardsley, J. M. & Vogel, C. R. (2003). *SIAM J. Sci. Comput.* **25**, 1326–1343.
- Bukharova, T. I. & Savyolova, T. I. (1985a). *Ind. Lab.* **51**, 56–60.
- Bukharova, T. I. & Savyolova, T. I. (1985b). *J. Appl. Math. Math. Phys.* **25**, 617–622.
- Bunge, H. J. (1965). *Z. Metallkd.* **56**, 872–874.
- Eschner, T. (1993). *Textures Microstruct.* **21**, 139–146.
- Eschner, T. (1994). *Textures in Geological Materials*, edited by H. J. Bunge, S. Siegesmund, W. Skrotzki & K. Weber, pp. 15–28, Proceedings of a Workshop. Oberursel: DGM Informationsgesellschaft.
- Grewen, J. & Wassermann, G. (1955). *Acta Metall.* **3**, 354–360.
- Helgason, S. (1984). *Groups and Geometric Analysis*. San Diego: Academic Press.
- Helgason, S. (1999). *The Radon Transform*, 2nd ed. Boston: Birkhäuser.
- Helming, K. & Eschner, T. (1990). *Cryst. Res. Technol.* **25**, K203–K208.
- Helming, K., Matthies, S. & Vinel, G. W. (1988). *Proceedings of the 8th International Conference on Textures of Materials 1987*, edited by J. S. Kallend & G. Gottstein, pp. 55–60. Littleton: American Institute of Mining, Metallurgical, and Petroleum Engineers.
- Hielscher, R. (2007). PhD Thesis, TU Freiberg, Germany.
- Hielscher, R., Bernstein, S., Schaeben, H., Boogaart, K. G. V. D., Beckmann, J. & Prestin, J. (2005). *Mater. Sci. Forum*, **495–497**, 313–318.
- Hielscher, R. & Schaeben, H. (2006). Proceedings IAMG 2006, Liège, September 3–8, 2006, CD S06-12, 1p.
- Lücke, K., Pospiech, J., Jura, J. & Hirsch, J. (1986). *Z. Metallkd.* **77**, 312–321.
- Lücke, K., Pospiech, J., Virnich, K. H. & Jura, J. (1981). *Acta Metall.* **29**, 167–182.
- Matthies, S. (1979). *Phys. Status Solidi B*, **92**, K135–K138.
- Nikolayev, D. I., Savyolova, T. I. & Feldmann, K. (1992). *Textures Microstruct.* **19**, 9–27.
- Roe, R. J. (1965). *J. Appl. Phys.* **36**, 2024–2031.
- Schaeben, H. (1996). *J. Appl. Cryst.* **29**, 516–525.
- Schaeben, H. (1997). *Phys. Status Solidi B*, **200**, 367–376.
- Schaeben, H. (1999). *Textures Microstruct.* **33**, 365–373.
- Schaeben, H. (2000). *J. Struct. Geol.* **22**, 1565–1568.
- Schaeben, H. & Boogaart, K. G. V. D. (2003). *Tectonophysics*, **370**, 253–268.
- Tarkowski, L., Laskosz, L. & Bonarski, J. T. (2004). *Mater. Sci. Forum*, **443–444**, 137–140.
- Virnich, K. H., Pospiech, J., Flemmer, A. & Lücke, K. (1978). *Proceedings of ICOTOM 5*, edited by G. Gottstein & K. Lücke, pp. 129–138. Berlin: Springer Verlag.